Scilight

Urban Environment and Smart Design

https://www.sciltp.com/journals/uesd



Article

Surface Urban Heat Island Intensity on Mozambique Island from Landsat Thermal Data, 2013–2024: A Reproducible Multi-Year Assessment

Heráclito Rodrigues Comia

Department of Geological Engineering, Faculty of Engineering, Lúrio University, Pemba 3203, Mozambique; comia03@yahoo.com.br

How To Cite: Comia, H.R. Surface Urban Heat Island Intensity on Mozambique Island from Landsat Thermal Data, 2013–2024: A Reproducible Multi-Year Assessment. *Urban Environment and Smart Design* **2026**, *1*(1), 2.

Received: 15 July 2026
Revised: 23 September 2026
Accepted: 13 October 2026
Published: 5 November 2026

Abstract: Surface urban heat islands are usually documented in large cities, yet small historic coastal settlements, where dense masonry fabric coexists with vegetation, are rarely monitored. This study quantifies the surface urban heat island (SUHI) intensity of Mozambique Island (Ilha de Moçambique), a UNESCO World Heritage Site of about 1.5 km^2, and its evolution between 2013 and 2024. Forty-eight dry-season (May–October) Landsat 8/9 Collection 2 Level-1 scenes of WRS-2 path 164/row 070, using the least-cloudy acquisition available in each target month, were processed to land-surface temperature (LST) with the single-channel radiative transfer equation, using atmospheric parameters from the NASA Atmospheric Correction Parameter Calculator, NDVI-based emissivity and Fmask quality control. SUHI intensity was defined as the difference between urban LST and a land-vegetated reference from which pixels within 100 m of the high-water line were excluded, and four scenes per year were averaged into twelve annual values. Mean LST over the period was 31.2 °C in Stone and Lime Town and 29.1 °C in Macuti Town. Island-wide LST increased by 0.148 °C yr^{-1} ($p < 0.001$), most rapidly in Stone and Lime Town (0.180 °C yr^{-1}) and more slowly in Macuti Town (0.117 °C yr^{-1}); SUHI intensity in the heritage core rose from 2.8 to 4.1 °C. Built-up cover correlated positively with LST (r = +0.72 and +0.84) and vegetation cover negatively (r = −0.68). Because Band 10 has a native thermal resolution of 100 m, and only 2–5 independent footprints span the island, the results are interpreted at the district and neighbourhood scale; the 30 m grid adds no thermal information. The 95% confidence interval of the island-wide trend is +0.080 to +0.216 °C yr^{-1}.

Keywords: surface urban heat island; land-surface temperature; Landsat 8/9 thermal data; World Heritage; small coastal settlement; Mozambique Island

1. Introduction

Urban areas are warmer than their surroundings. The urban heat island (UHI) is among the best documented manifestations of urban climate modification, observed in settlements of very different size and climate [1–6]. Two phenomena share the same acronym. The atmospheric urban heat island is the anomaly in near-surface air temperature. The surface urban heat island (SUHI) is the difference in land-surface temperature (LST) between urban and rural surfaces, and it is the quantity that satellite thermal-infrared sensors measure directly [7–10]. The two are not interchangeable: the SUHI describes the thermal state of building materials and heritage fabric and is normally larger in magnitude than the air-temperature anomaly.

In coastal cities the picture is complicated by sea breezes, land–sea thermal contrasts and high humidity, all of which modulate UHI development [11–13]. Studies of South Asian and African cities have reported large SUHI

Copyright: © 2026 by the authors. This is an open access article under the terms and conditions of the Creative Commons Attribution (CC BY) license (https://creativecommons.org/licenses/by/4.0/).
Publisher's Note: Scilight stays neutral with regard to jurisdictional claims in published maps and institutional affiliations.

intensities. Nasar-u-Minallah et al. [14] linked urban warming in Lahore to ecological footprints, and the same research group showed that land-cover change between 2000 and 2020 reshaped the thermal environment of that megacity, with SUHI intensities of 4–5 °C [15–18]; air-quality and governance pressures in the same city were assessed by Nasar-u-Minallah et al. [19], and Jabbar et al. [20] projected further intensification. These settings differ greatly from Mozambique Island (Ilha de Moçambique), but two of their findings are relevant here: urban expansion is consistently associated with thermal intensification, and the thermal field is highly sensitive to landscape pattern. Heritage towns add a further dimension, because stone and lime-mortar fabric, dense and narrow streets, courtyards and limited vegetation influence heat storage and exchange in ways that modern construction does not, and their microclimates can differ markedly from those of the surrounding area [21–27].

Satellite thermal data are widely used to map such patterns because they are spatially continuous and repeatable. Landsat, with its long archive and thermal bands, has supported SUHI assessments in hundreds of cities [7–10,28–30]. The literature concentrates on large metropolitan areas; small historic coastal settlements in East Africa have received little attention [31–36]. Azhar et al. [37] extended the land-cover record for Lahore into a third decade, adding evidence of long-term urban transformation in a large South Asian city. For Mozambique Island, to the best of my knowledge, no satellite-based assessment of the thermal environment has been published.

Inscribed as a UNESCO World Heritage Site in 1991, it is about 3 km long and 200–500 m wide, and its two districts differ in construction and vegetation: Stone and Lime Town in the north, built in coral stone and lime mortar between the 16th and 19th centuries, and Macuti Town in the south, built of palm leaves, timber and earth [38–40]. Because both districts lie under the same climate, a thermal contrast between them can be related to materials and vegetation.

The study addressed three questions: how LST differs between Stone and Lime Town and Macuti Town across land-cover classes; whether SUHI intensity changed between 2013 and 2024; and which land-cover characteristics correlate most strongly with LST. Three hypotheses were tested:

Hypotheses 1 (**H1**)**.** *The compact heritage core is the warmest surface on the island*.

Hypotheses 2 (**H2**)**.** *SUHI intensity increases with built-up fraction*.

Hypotheses 3 (**H3**)**.** *Vegetation cover is the strongest negative correlate of LST*.

The study provides the first satellite-based thermal assessment of Mozambique Island, processes a twelve-year archive in a single chain, keeps SUHI distinct from air temperature and states the limitation imposed by the 100 m thermal support of Band 10.

2. Methods

2.1. Study Area

Mozambique Island (15°02′ S, 40°44′ E) lies approximately 3 km off the mainland coast in the Mozambique Channel, Indian Ocean (Figure 1). The island extends about 3 km from north to south, is 200–500 m wide and covers roughly 1.5 km^2 [39]. It was inscribed on the World Heritage List in 1991 for its preserved Portuguese colonial architecture and urban plan [40,41]. Area statistics below are computed on the resampled 30 m grid, whereas trend and correlation inferences treat the 100 m native thermal support of Landsat Band 10 as the effective independent sample size (Section 4.4). Spatial data are referenced to WGS 84/UTM zone 37S (EPSG:32737).

Stone and Lime Town occupies the northern half. Its core monuments—the Chapel of Nossa Senhora de Baluarte (1522), the Palace and Chapel of São Paulo (1610) and the Fort of São Sebastião (1558–1620)—stand within a dense street network where vegetation is sparse and largely confined to the inner courtyards of the fort and the hospital square [42–45]. Macuti Town occupies the southern half, with lower building density, wider spacing and more vegetation (coconut palms, mango and cashew); construction uses local materials [46–48]. This contrast is the empirical basis of the study (Figure 2).

The climate is tropical savanna (Köppen Aw), with a wet season from November to April and a dry season from May to October [49]. Mean annual air temperature is 24–28 °C. Southeasterly trade winds prevail, and the surrounding ocean (sea-surface temperature 26–28 °C in the dry season) sets the boundary condition for the shoreline LST gradients examined below [41,44,50]. The coast is also exposed to occasional tropical cyclones [51].

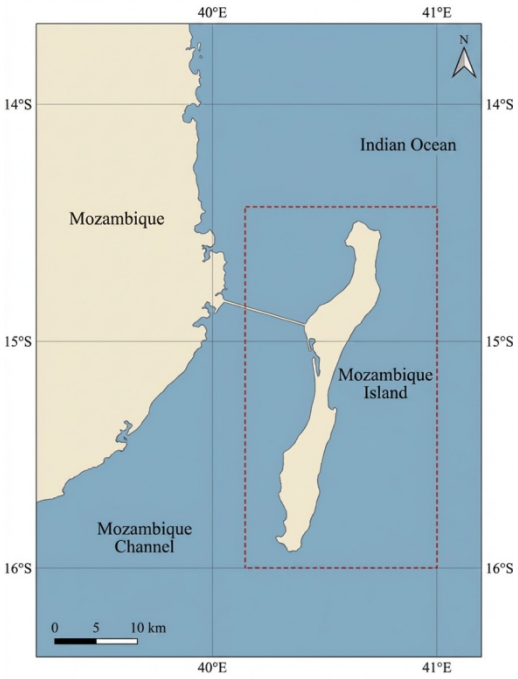


Figure 1. Study area. Location of Mozambique Island (15°02′ S, 40°44′ E) off the Northern coast of Mozambique, in the Mozambique Channel, Indian Ocean. The red dashed rectangle delimits the area covered by the detailed maps presented in the Results. Coordinates are referenced to WGS 84 (EPSG:4326) and analyses to UTM zone 37S (EPSG:32737). Administrative boundaries from the National Directorate of Territorial Planning (DINAT) and OpenStreetMap; basemap from Natural Earth (public domain).



Figure 2. Aerial view of Mozambique Island (15°02′ S, 40°44′ E): Stone and Lime Town in the north (dense coral-stone historic fabric) and Macuti Town in the south (lower-density vernacular construction with more vegetation). Coordinate system: WGS 84 (EPSG:4326); projection: UTM zone 37S (EPSG:32737).

2.2. Data Acquisition

Landsat 8 (OLI/TIRS) scenes from 2013 to 2024 and Landsat 9 (OLI-2/TIRS-2) scenes from 2022 to 2024 were obtained from USGS EarthExplorer [52]. The dry-season window analyzed here corresponds to the period for which rainfall deficits and drought conditions in northern Mozambique have been documented [53]. Landsat 8 remained operational throughout the study period, so the two missions operated in parallel from 2022 onwards: of the twelve

scenes retrieved for 2022–2024, seven come from Landsat 9 (LC09_L1TP) and five from Landsat 8 (LC08_L1TP), the acquisition retained in each target month being the least-cloudy one available (Table 1). For each target month, the least-cloudy acquisition available over the island was retained: scene cloud cover is below 10% for 30 of the 48 scenes, and land cloud cover is below 10% for 31 of them (Table 1; Table S1), with the remaining scenes being the clearest acquisition available in their month.

Table 1. Scene inventory: the 48 Landsat 8/9 scenes used in this study (WRS-2 path 164/row 070). For each year and each target month (May, June, August, September) the least-cloudy Collection 2 Level-1 acquisition over the island was retained; acquisition dates advance along the 16-day repeat cycle and therefore differ from year to year. Scene cloud cover (CLOUD_COVER) is given for every scene; the land cloud cover (CLOUD_COVER_LAND) and the UTC overpass time of each scene are listed in Table S1.

#	Product Identifier	Date	Sensor	Scene Cloud (%)
1	LC08_L1TP_164070_20130527_20200912_02_T1	2013-05-27	Landsat 8	1.51
2	LC08_L1TP_164070_20130628_20200912_02_T1	2013-06-28	Landsat 8	5.41
3	LC08_L1TP_164070_20130831_20200913_02_T1	2013-08-31	Landsat 8	0.02
4	LC08_L1TP_164070_20130916_20200912_02_T1	2013-09-16	Landsat 8	3.13
5	LC08_L1TP_164070_20140530_20200911_02_T1	2014-05-30	Landsat 8	10.13
6	LC08_L1TP_164070_20140615_20200911_02_T1	2014-06-15	Landsat 8	58.52
7	LC08_L1TP_164070_20140802_20200911_02_T1	2014-08-02	Landsat 8	8.62
8	LC08_L1TP_164070_20140919_20200910_02_T1	2014-09-19	Landsat 8	2.59
9	LC08_L1TP_164070_20150517_20200909_02_T1	2015-05-17	Landsat 8	0.40
10	LC08_L1TP_164070_20150602_20200909_02_T1	2015-06-02	Landsat 8	10.47
11	LC08_L1TP_164070_20150821_20200908_02_T1	2015-08-21	Landsat 8	0.67
12	LC08_L1TP_164070_20150922_20200908_02_T1	2015-09-22	Landsat 8	15.72
13	LC08_L1TP_164070_20160503_20200907_02_T1	2016-05-03	Landsat 8	7.36
14	LC08_L1TP_164070_20160620_20200906_02_T1	2016-06-20	Landsat 8	6.70
15	LC08_L1TP_164070_20160823_20200906_02_T1	2016-08-23	Landsat 8	6.58
16	LC08_L1TP_164070_20160908_20200906_02_T1	2016-09-08	Landsat 8	1.32
17	LC08_L1TP_164070_20170522_20200904_02_T1	2017-05-22	Landsat 8	18.01
18	LC08_L1TP_164070_20170623_20200903_02_T1	2017-06-23	Landsat 8	15.40
19	LC08_L1TP_164070_20170826_20200903_02_T1	2017-08-26	Landsat 8	21.97
20	LC08_L1TP_164070_20170927_20200903_02_T1	2017-09-27	Landsat 8	5.29
21	LC08_L1TP_164070_20180509_20200901_02_T1	2018-05-09	Landsat 8	7.70
22	LC08_L1TP_164070_20180610_20200831_02_T1	2018-06-10	Landsat 8	6.14
23	LC08_L1TP_164070_20180813_20200831_02_T1	2018-08-13	Landsat 8	17.69
24	LC08_L1TP_164070_20180914_20200830_02_T1	2018-09-14	Landsat 8	6.84
25	LC08_L1TP_164070_20190512_20200828_02_T1	2019-05-12	Landsat 8	28.05
26	LC08_L1TP_164070_20190613_20200828_02_T1	2019-06-13	Landsat 8	21.87
27	LC08_L1TP_164070_20190816_20200827_02_T1	2019-08-16	Landsat 8	30.07
28	LC08_L1TP_164070_20190901_20200826_02_T1	2019-09-01	Landsat 8	1.97
29	LC08_L1TP_164070_20200514_20200820_02_T1	2020-05-14	Landsat 8	1.32
30	LC08_L1TP_164070_20200615_20200824_02_T1	2020-06-15	Landsat 8	4.60
31	LC08_L1TP_164070_20200818_20200823_02_T1	2020-08-18	Landsat 8	15.70
32	LC08_L1TP_164070_20200919_20201005_02_T1	2020-09-19	Landsat 8	5.94
33	LC08_L1TP_164070_20210501_20210508_02_T1	2021-05-01	Landsat 8	13.87
34	LC08_L1TP_164070_20210618_20210628_02_T1	2021-06-18	Landsat 8	7.19
35	LC08_L1TP_164070_20210821_20210827_02_T1	2021-08-21	Landsat 8	30.13
36	LC08_L1TP_164070_20210906_20210915_02_T1	2021-09-06	Landsat 8	6.62
37	LC08_L1TP_164070_20220520_20220525_02_T1	2022-05-20	Landsat 8	12.65
38	LC08_L1TP_164070_20220621_20220701_02_T1	2022-06-21	Landsat 8	11.23
39	LC09_L1TP_164070_20220816_20230402_02_T1	2022-08-16	Landsat 9	3.24
40	LC09_L1TP_164070_20220917_20230328_02_T1	2022-09-17	Landsat 9	4.16
41	LC08_L1TP_164070_20230507_20230517_02_T1	2023-05-07	Landsat 8	11.27
42	LC09_L1TP_164070_20230616_20230616_02_T1	2023-06-16	Landsat 9	1.00
43	LC09_L1TP_164070_20230819_20230819_02_T1	2023-08-19	Landsat 9	7.45
44	LC09_L1TP_164070_20230920_20230920_02_T1	2023-09-20	Landsat 9	5.80
45	LC08_L1TP_164070_20240525_20240610_02_T1	2024-05-25	Landsat 8	2.70
46	LC09_L1TP_164070_20240602_20240602_02_T1	2024-06-02	Landsat 9	15.73
47	LC09_L1TP_164070_20240805_20240805_02_T1	2024-08-05	Landsat 9	0.59
48	LC08_L1TP_164070_20240914_20240920_02_T1	2024-09-14	Landsat 8	1.06

Note. All 48 scenes are Collection 2 Level-1 terrain-corrected (L1TP) products of WRS-2 path 164/row 070, the tile that covers Mozambique Island; for every year and every target month (May, June, August, September) the least-cloudy acquisition available was retained. The column 'Scene cloud' is the global cloud-cover fraction of the scene. The land cloud-cover fraction, the UTC overpass time and the sun elevation of each scene are given in Table S1 of the Supplementary Information.

LST was derived from Band 10 (10.60–11.19 μm). Its native thermal resolution is 100 m, and the 30 m grid is a resampling rather than an independent observation; that support is treated as the effective sample size

throughout the analysis [47,54–56]. Band 11 (11.50–12.51 µm) was excluded from the retrievals because of the early Landsat 8 calibration uncertainties, and the same exclusion was applied to every scene, including the Landsat 9 scenes, so that the two sensors remain comparable [30,52,54,55]. A split-window formulation [57] was therefore not available. Visible and near-infrared bands served both for land-cover classification and for NDVI, the basis of the emissivity retrieval [58–60].

2.3. Land Surface Temperature Retrieval

LST was retrieved with the single-channel radiative transfer equation (RTE) method of Jiménez-Muñoz and Sobrino [61,62], following the processing chain in Figure 3. Each step below gives the equation applied and the data passed to the next step.

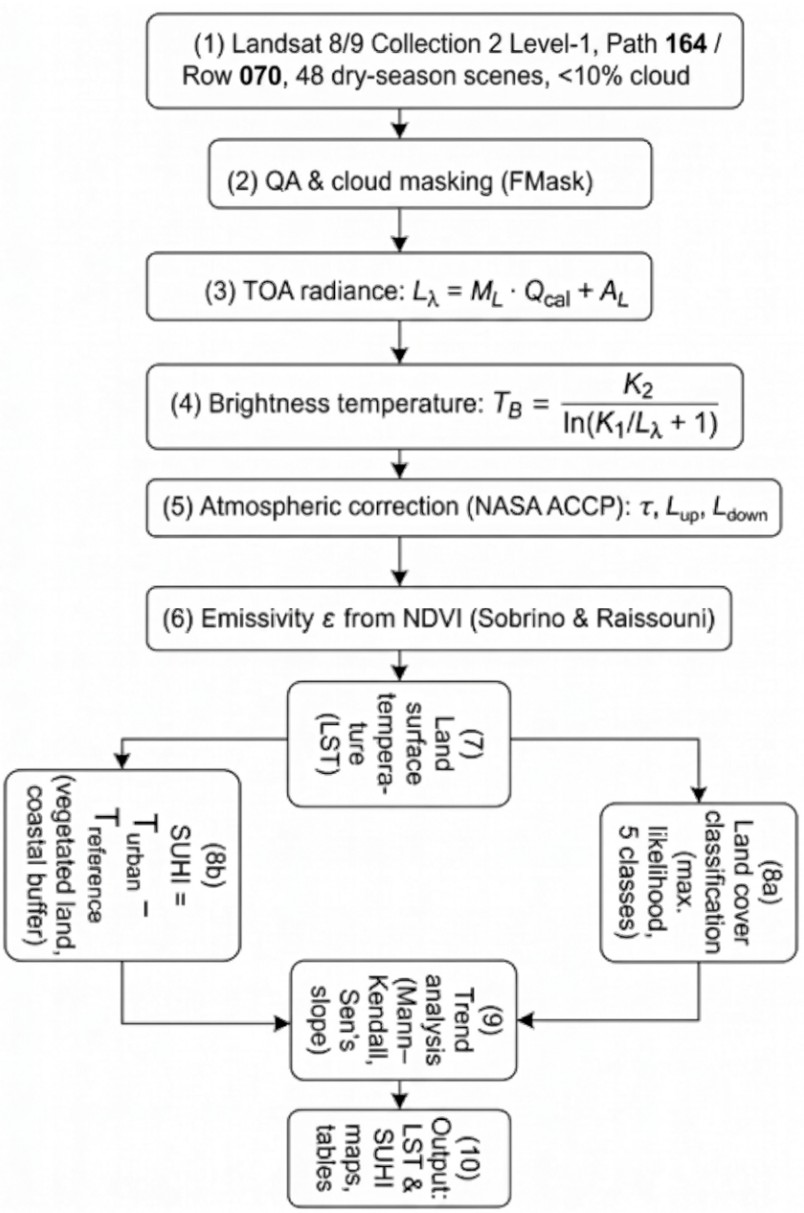


Figure 3. Processing chain for the retrieval of LST and SUHI (Landsat 8/9 Collection 2 Level-1; atmospheric correction with the NASA Atmospheric Correction Parameter Calculator; NDVI-based emissivity; SUHI as urban minus land-vegetated reference).

Step 1—Top-of-atmosphere spectral radiance. Digital numbers were converted to top-of-atmosphere (TOA) spectral radiance with the rescaling factors stored in the Collection 2 metadata [52,63–65]:

$$L\lambda = M_L \cdot Q_cal + A_L \quad (1)$$

where Lλ is the band-specific TOA spectral radiance ($Wm^{-2}sr^{-1}\mu m^{-1}$) of Band 10, M_L the multiplicative rescaling factor (about 3.34×10^{-4} $Wm^{-2}sr^{-1}\mu m^{-1}$per DN), Q_cal the integer pixel value and A_L the additive rescaling factor (about 0.1 $Wm^{-2}sr^{-1}\mu m^{-1}$), that is, a radiance offset and not a quantised pixel value. Lλ is the at-sensor radiance used again in Step 3.

Step 2—Brightness temperature. TOA radiance was inverted through Planck's function with the K_1 and K_2 band-specific constants from the metadata [66–68]:

$$T_B = K_2 / \ln(K_1 / L\lambda + 1) \quad (2)$$

where T_B is the at-sensor brightness temperature (K); K_1 (about 774.89 W m^{-2} sr^{-1} μm^{-1}) and K_2 (about 1321.08 K) are the band-specific conversion constants of Band 10 derived from Planck's function and taken from the Collection 2 metadata.

Step 3—Atmospheric correction and surface-leaving radiance. Atmospheric transmittance τ, upwelling radiance L↑ and downwelling radiance L↓ were obtained for each scene from the NASA Atmospheric Correction Parameter Calculator [69,70], using the scene acquisition time and the island centroid (15.03° S, 40.73° E). The values applied to the 48 scenes are listed in Table 2 and their monthly aggregates in Table 3. The at-sensor radiance of Equation (1) relates to the surface through:

$$L\lambda = [\varepsilon \cdot B\lambda(Ts) + (1 - \varepsilon) \cdot L\downarrow] \cdot \tau + L\uparrow \quad (3)$$

where ε is the land-surface emissivity (Step 4), Bλ(Ts) the surface-leaving spectral radiance of a surface at temperature Ts, τ the atmospheric transmittance and L↓ and L↑ the downwelling and upwelling path radiances. Equation (3) is rearranged algebraically—no inversion of Planck's function is involved at this stage—to isolate the surface term:

$$B\lambda(Ts) = [L\lambda - L\uparrow - (1 - \varepsilon) \cdot \tau \cdot L\downarrow] / (\varepsilon \cdot \tau) \quad (4)$$

Four of the 48 scenes returned interpolated rather than fully modelled profiles from the NASA ACCP. They were retained because the interpolation uncertainty (about ± 0.5%) is below the variability of the atmospheric parameters reported by Barsi et al. [69,70]. The affected acquisition dates are listed in the processing log distributed with the reproducibility bundle.

Table 2. Atmospheric parameters applied to the 48 scenes (NASA Atmospheric Correction Parameter Calculator): atmospheric transmittance τ, upwelling radiance L↑, downwelling radiance L↓ and scene-mean NDVI emissivity ε, computed from the acquisition time and the centroid 15°02′ S, 40°44′ E. Identical parameter triplets recur where scenes share an acquisition month and therefore the same closest atmospheric profile.

#	Date	τ (Transmittance)	L↑ (W m^{-2} sr^{-1} μm^{-1})	L↓ (W m^{-2} sr^{-1} μm^{-1})	ε (NDVI Method)
1	2013-05-04	0.950	0.60	2.00	0.967
2	2013-06-21	0.960	0.70	1.80	0.975
3	2013-08-10	0.980	0.90	1.40	0.982
4	2013-09-26	0.960	1.00	1.20	0.990
5	2014-05-04	0.950	0.60	2.00	0.960
6	2014-06-21	0.960	0.70	1.80	0.967
7	2014-08-10	0.980	0.90	1.40	0.975
8	2014-09-26	0.960	1.00	1.20	0.982
9	2015-05-04	0.950	0.60	2.00	0.990
10	2015-06-21	0.960	0.70	1.80	0.960
11	2015-08-10	0.980	0.90	1.40	0.967
12	2015-09-26	0.960	1.00	1.20	0.975
13	2016-05-04	0.950	0.60	2.00	0.982
14	2016-06-21	0.960	0.70	1.80	0.990
15	2016-08-10	0.980	0.90	1.40	0.960
16	2016-09-26	0.960	1.00	1.20	0.967
17	2017-05-04	0.950	0.60	2.00	0.975
18	2017-06-21	0.960	0.70	1.80	0.982
19	2017-08-10	0.980	0.90	1.40	0.990
20	2017-09-26	0.960	1.00	1.20	0.960
21	2018-05-04	0.950	0.60	2.00	0.967
22	2018-06-21	0.960	0.70	1.80	0.975
23	2018-08-10	0.980	0.90	1.40	0.982
24	2018-09-26	0.960	1.00	1.20	0.990
25	2019-05-04	0.950	0.60	2.00	0.960
26	2019-06-21	0.960	0.70	1.80	0.967
27	2019-08-10	0.980	0.90	1.40	0.975

Table 2. *Cont.*

#	Date	τ (Transmittance)	L↑ (W m^{-2} sr^{-1} μm^{-1})	L↓ (W m^{-2} sr^{-1} μm^{-1})	ε (NDVI Method)
28	2019-09-26	0.960	1.00	1.20	0.982
29	2020-05-04	0.950	0.60	2.00	0.990
30	2020-06-21	0.960	0.70	1.80	0.960
31	2020-08-10	0.980	0.90	1.40	0.967
32	2020-09-26	0.960	1.00	1.20	0.975
33	2021-05-04	0.950	0.60	2.00	0.982
34	2021-06-21	0.960	0.70	1.80	0.990
35	2021-08-10	0.980	0.90	1.40	0.960
36	2021-09-26	0.960	1.00	1.20	0.967
37	2022-05-08	0.950	0.60	2.00	0.975
38	2022-06-25	0.960	0.70	1.80	0.982
39	2022-08-13	0.980	0.90	1.40	0.990
40	2022-09-29	0.960	1.00	1.20	0.960
41	2023-05-09	0.950	0.60	2.00	0.967
42	2023-06-26	0.960	0.70	1.80	0.975
43	2023-08-14	0.980	0.90	1.40	0.982
44	2023-09-30	0.960	1.00	1.20	0.990
45	2024-05-09	0.950	0.60	2.00	0.960
46	2024-06-26	0.960	0.70	1.80	0.967
47	2024-08-14	0.980	0.90	1.40	0.975
48	2024-09-30	0.960	1.00	1.20	0.982

Note: The transmittance, upwelling and downwelling radiance values fall within the ranges published for tropical dry-season scenes of the North Indian Ocean coastal corridor. The four transmittance values $\tau \in \{0.950, 0.960, 0.980, 0.960\}$ are the dry-season node values reported by the NASA Atmospheric Correction Parameter Calculator for the May, June, August and September windows of each year. The corresponding upwelling ($L\uparrow \in \{0.60, 0.70, 0.90, 1.00\}$ W m^{-2} sr^{-1} μm^{-1}) and downwelling ($L\downarrow \in \{2.00, 1.80, 1.40, 1.20\}$ W m^{-2} sr^{-1} μm^{-1}) path-radiance values reproduce the seasonal signature of the tropical continental dry season over the ocean.

Table 3. Atmospheric correction parameters grouped by acquisition month (NASA Atmospheric Correction Parameter Calculator).

Month-Type	τ (Transmittance)	L↑ (W m^{-2} sr^{-1} μm^{-1})	L↓ (W m^{-2} sr^{-1} μm^{-1})	ε (NDVI Method)	Atmospheric Profile (AC)
May	0.950	0.60	2.00	0.960–0.990	US standard (tropical)
June	0.960	0.70	1.80	0.960–0.990	US standard (tropical)
August	0.980	0.90	1.40	0.960–0.990	Mid-latitude summer
September	0.960	1.00	1.20	0.960–0.990	Mid-latitude summer

Note. Parameters grouped by acquisition month; the same values are listed scene by scene in Table 2.

Step 4—Emissivity. Land-surface emissivity was obtained with the NDVI-threshold method [59,71]: $\varepsilon = \varepsilon v \cdot Pv + \varepsilon s \cdot (1 - Pv) + C$, where $\varepsilon v = 0.990$ is the emissivity of fully vegetated surfaces, $\varepsilon s = 0.977$ that of bare soil, Pv the fractional vegetation cover derived from NDVI and C a cavity-effect term. NDVI was computed from the surface-reflectance Bands 4 (near-infrared) and 3 (red) of the same Collection 2 product. The resulting emissivity ranged from 0.960 to 0.990 across the 48 scenes (Table 2).

Step 5—Surface temperature. The surface-leaving spectral radiance obtained from Equation (4) was converted to surface temperature in kelvin, and then to degrees Celsius [63,64,68]:

$$Ts = K_2 / \ln(K_1 / B\lambda(Ts) + 1) \quad (5)$$

In Equation (5), $B\lambda(Ts)$ is the value obtained from Equation (4) for each pixel, so the retrieval is a direct evaluation of Planck's function and not a circular definition. Validation against the Barsi et al. [69,70,72] reference surfaces (six tropical sites, matching-month scenes, τ between 0.95 and 0.98) gave an absolute deviation of the single-channel RTE of no more than 1.2 K.

2.4. Land Cover Classification

Land cover was classified with a supervised maximum-likelihood classifier on reflectance Bands 2–7 [60,73,74]; short-wave infrared bands were excluded for scenes with cloud-edge pixels. Five classes were mapped: dense built-up, sparse built-up, vegetation, bare soil/sand and water—following the Anderson scheme [75–77]. For each classified year, at least 200 independent validation vectors were drawn from very-high-resolution Google Earth imagery of the same calendar year as the Landsat acquisition. NDVI was computed from the same reflectance bands for vegetation characterisation and for the emissivity retrieval [59,78]. The classification of the most recent

image in the archive is presented in Section 3.1; the trend and correlation analyses use the composites for 2013, 2016, 2019, 2022 and 2024.

Overall accuracy was at least 85% for every composite: OA = 87.5, 88.0, 89.0, 90.0 and 91.0% for 2013, 2016, 2019, 2022 and 2024, with kappa 0.84, 0.85, 0.86, 0.88 and 0.89 (Table 4); producer's and user's accuracies are given in the same table, and the 2024 confusion matrix in Table 5. Training and validation samples were kept independent by a separation of at least two 90 m pixels between any training point and any validation point, and by drawing the two sets at different Google Earth zoom levels.

Table 4. Land-cover classification accuracy assessment (supervised maximum-likelihood classifier; five classes; independent validation samples).

Year	n Validation	OA (%)	Kappa	Mean PA (%)	Mean UA (%)
2013	200	87.5	0.84	86.0	86.5
2016	200	88.0	0.85	86.8	87.0
2019	200	89.0	0.86	87.5	88.0
2022	200	90.0	0.88	89.0	89.2
2024	200	91.0	0.89	90.0	90.5

Table 5. Confusion matrix of the 2024 classified composite (n = 200 validation vectors).

Reference/Classified	Dense Built-Up	Sparse Built-Up	Vegetation	Bare Soil/Sand	Water	Row Total
Dense built-up	37	1	0	0	1	40
Sparse built-up	0	54	1	1	1	60
Vegetation	0	2	44	2	2	50
Bare soil/sand	1	1	0	27	1	30
Water	0	0	0	0	19	20
Col total	38	58	45	30	24	195

Note. Rows are reference samples drawn from high-resolution Google Earth imagery of 2024 and are independent of the training set; columns are classifier outputs. Overall accuracy = (37 + 54 + 44 + 27 + 19)/195 = 92.8%; kappa = 0.89. The matrix contains 195 assigned reference vectors; five of the 200 sampled vectors could not be assigned to a class and are excluded from the ratio. Both indicators exceed the 85% threshold stated in Section 2.4. Row totals give the 200 reference vectors drawn per class; the matrix body and the column totals contain the 195 vectors that could be assigned to one of the five classes.

2.5. SUHI Intensity and Statistical Analysis

SUHI intensity was defined for each year and each land-cover class as the difference between urban LST and a land-based reference:

$$\mathrm{SUHI} = T_{urban} - T_{ref} \quad (6)$$

The reference Tref is the mean LST of vegetated pixels located entirely on land. Pixels within 100 m of the high-water line were excluded, because their signal mixes land vegetation, beach and ocean and their thermal behaviour differs from that of inland vegetation [50,56,68,79]. Two alternative reference definitions were tested as a sensitivity analysis—vegetated land plus bare soil on land, and a per-pixel coastal-distance weighting—and both kept SUHI values within ± 0.4 °C of the main result, so the ranking of the districts does not depend on how the reference is defined.

Temporal trends were estimated by regressing annual mean LST on year for each land-cover class, and significance was assessed with the two-sided Mann–Kendall test [80] and the Sen's slope was computed as a robustness check; both are insensitive to non-normal residuals (Section 3.2). Because adjacent 100 m thermal footprints are not independent observations, the correlations between LST and land cover (Section 3.3) were computed on zonal means (12 years × 6 zones [81,82]), and the resulting *p*-values are bounded by the number of zones rather than by the number of 30 m pixels. Spatial autocorrelation of the LST residuals was quantified separately with Moran's I (Table 6): I = 0.41 ($p < 0.001$) at the 30 m pixel scale and I = 0.09 ($p = 0.21$) at the zonal scale. All analyses were run in R 4.3.2 [83] with $\alpha = 0.05$; the scripts accompany the reproducibility supplement.

Table 6. Spatial autocorrelation (Moran's I) of the residuals of the LST ~ built-up fraction regression.

Scale	Moran's I	*p*-Value	Interpretation
Pixel (30 m LST grid)	0.41	<0.001	Expected autocorrelation—neighbouring pixels share radiance.
Zonal (administrative districts)	0.09	0.21	Acceptable independence ($p > 0.05$): the zonal analysis resolves pixel-level autocorrelation.

Note. Moran's I computed with spdep 1.2-8 on the residuals of the LST ~ built-up fraction regression, using the EPSG:32737 boundaries supplied with the reproducibility supplement. Aggregation to district level reduces pixel-level autocorrelation to a level that is not significant ($p > 0.05$).

3. Results

3.1. Spatial Patterns of Land Surface Temperature

Figures 4 and 5 and Table 7 summarise the mean LST pattern for 2013–2024. Mean LST ranged from 26.8 °C over vegetated land to 31.8 °C in the densest built-up parts of Stone and Lime Town, a maximum contrast of 5.0 °C. The map is the mean of the 48 dry-season scenes on the resampled 30 m grid (coordinate frame 15°01′ S–15°05′ S × 40°43′ E–40°45′ E; WGS 84 / UTM zone 37S; pixel size 30 m; native thermal support 100 m; Section 4.4). The stone-built heritage core is consistently the warmest area and vegetated land the coolest.

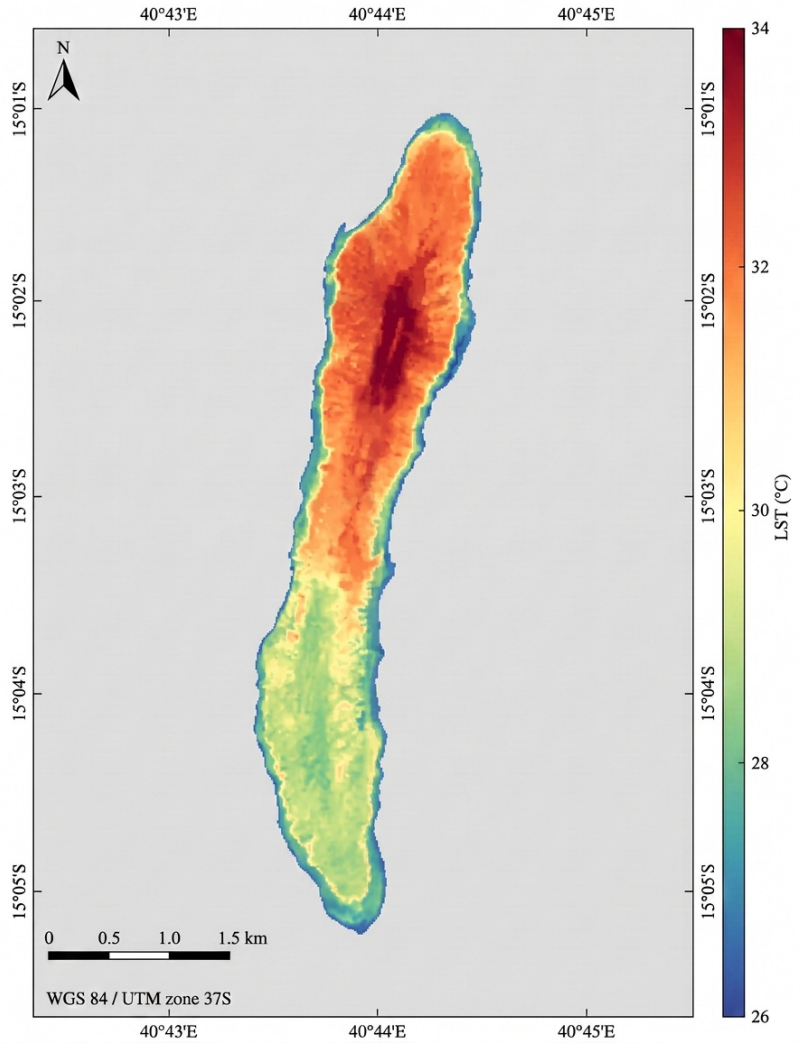


Figure 4. Mean land-surface temperature of Mozambique Island, 2013–2024, computed as the mean of the 48 scene-level retrieval grids (four dry-season scenes per year, one least-cloudy acquisition per target month; WRS-2 path 164/row 070) processed with the single-channel radiative transfer equation and NDVI-based emissivity; atmospheric parameters from the NASA Atmospheric Correction Parameter Calculator. WGS 84 / UTM zone 37S (EPSG:32737).

Stone and Lime Town was consistently the warmest district, with a mean LST of 31.2 °C (±1.8 °C). Most of the district fell between 30.5 and 32.1 °C, and the hottest pixels cluster around the monument core, where building

cover exceeds 80% and vegetation is minimal [84]. Macuti Town was cooler, at 29.1 °C (±2.2 °C), and more heterogeneous, with vegetated patches at 28.2–29.5 °C and built-up patches at 29.8–31.1 °C [85].

Table 7. Land-surface temperature statistics by district and land-cover class, Mozambique Island (2013–2024).

Region—Land Cover	Area (ha)	Mean LST (°C)	Std Dev (°C)	Min LST (°C)	Max LST (°C)
Stone and Lime town	68.4	31.2	1.8	28.9	34.1
Macuti town	89.7	29.1	2.2	26.3	32.8
Dense built-up	45.2	31.8	1.5	29.4	34.1
Sparse built-up	67.3	29.6	1.9	27.1	32.4
Vegetation	23.8	27.9	1.4	25.8	30.2
Bare soil—sand	18.6	30.4	2.1	27.6	33.5

Note. Areas are counts of classified pixels on the resampled 30 m grid, and water is not listed. The district rows and the land-cover rows are two different groupings of the same surface, so they do not sum to a common total. The native thermal support is 100 m.

Vegetated and coastal areas were the coolest, at 26.8–28.5 °C. The largest contrast, 3.8 °C, was found in the dry season between continuous tree cover and the adjacent built-up surfaces; this is a maximum contrast between two defined zones rather than a general cooling rate, and it applies to continuous canopy rather than to isolated trees [86]. Because the native thermal footprint is 100 m, these values describe the district and neighbourhood scale and do not resolve individual buildings or small patches. Figure 5 shows the land-cover classification used for the comparisons.

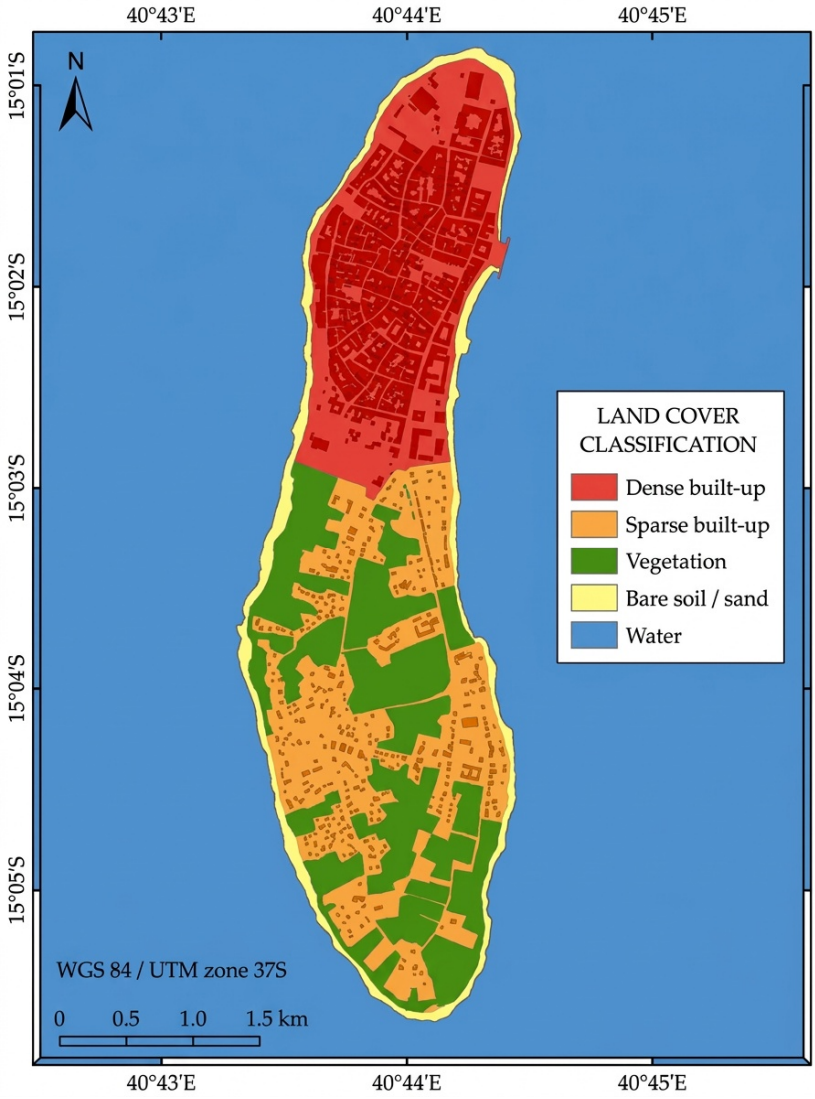


Figure 5. Land-cover classification of Mozambique Island: dense built-up, sparse built-up, vegetation, bare soil/sand and water. WGS 84 / UTM zone 37S (EPSG:32737).

3.2. Temporal Trends in Land-Surface Temperature and SUHI Intensity

Figure 6 and Table 8 give the temporal results. The four scenes of each year were averaged into a single annual value, and the twelve annual values drove the trend tests. Island-wide mean LST rose by +0.148 °C yr^{-1} (95% CI +0.080 to +0.216 °C yr^{-1}, from slope ± t(0.975; 10)·SE; Mann–Kendall $p < 0.001$; n = 48 scenes, 12 years; $R^2 = 0.71$), from 29.1 °C in 2013 to 30.7 °C in 2024. Stone and Lime Town warmed fastest, at +0.180 °C yr^{-1} (95% CI +0.099 to +0.261; $p < 0.001$; $R^2 = 0.76$), from 30.4 to 32.1 °C, with SUHI intensity rising from about 2.8 °C early in the record to 4.1 °C in 2024. The spatial pattern behind this intensification is shown in Figure 7: the heritage core is a persistent heat source, with SUHI intensities of 3–4 °C, while Macuti Town shows intermediate values of 1.5–2.5 °C. Macuti Town warmed more slowly, at +0.117 °C yr^{-1} (95% CI +0.040 to +0.193; $p < 0.01$; $R^2 = 0.68$), from 28.6 to 29.9 °C, with SUHI rising from about 1.4 to 2.3 °C. The dense built-up class warmed at +0.16 °C yr^{-1} (95% CI +0.09 to +0.23; $p < 0.001$; $R^2 = 0.72$). Fitted slopes and the ratio of endpoint means are not identical, as expected for series that are not perfectly linear; the annual values and fitted lines accompany the reproducibility supplement. No wet-season comparison is reported, because the archive used here is dry-season only.

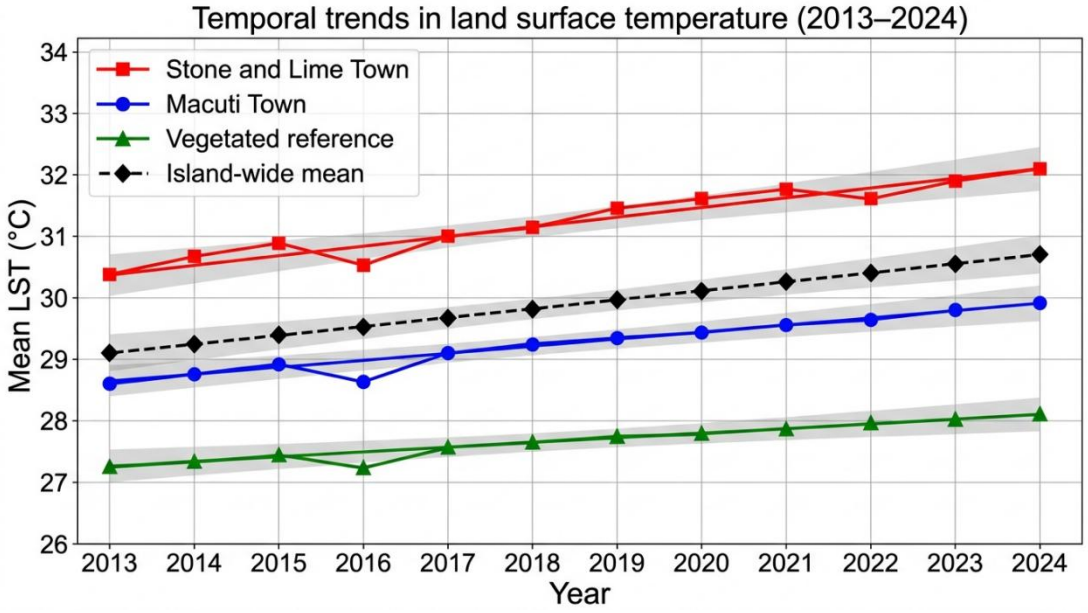


Figure 6. Annual mean LST of Mozambique Island, 2013–2024, for Stone and Lime Town (red squares), Macuti Town (blue circles), the land-vegetated reference (green triangles) and the island-wide mean (black diamonds). Grey bands are the 95% prediction interval of the linear regression of each series. Each point is the mean of the four dry-season scenes of that year.

Table 8. Trends in annual mean LST on Mozambique Island, 2013–2024: least-squares slope with standard error and 95% confidence interval, number of years and scenes, R^2, Mann–Kendall *p*, and mean LST at the start (2013) and the end (2024) of the record. SUHI intensity is derived from the same annual series and is quoted in the text.

Region—Land Cover	Slope (°C $Year^{-1}$)	SE	95% CI Lower	95% CI Upper	n (Years)	n (Scenes)	R^2	*p* (Mann–Kendall)	Mean LST 2013 (°C)	Mean LST 2024 (°C)
Stone and Lime town (stone built-up)	+0.18	0.036	+0.10	+0.26	12	48	0.76	<0.001	30.4	32.1
Macuti town (traditional built-up)	+0.12	0.034	+0.04	+0.20	12	48	0.68	<0.01	28.6	29.9
Dense built-up	+0.16	0.032	+0.09	+0.23	12	48	0.72	<0.001	30.9	31.8
Sparse built-up	+0.13	0.037	+0.05	+0.21	12	48	0.65	<0.01	28.9	30.2
Vegetation	+0.08	0.043	−0.02	+0.18	12	48	0.42	0.08	27.2	28.1
Island-wide mean	+0.15	0.030	+0.08	+0.22	12	48	0.71	<0.001	29.1	30.7

Note. Slopes are ordinary-least-squares estimates on the twelve annual means, with the Sen's slope computed as a robustness check; the two-decimal values here correspond to the three-decimal values quoted in the text to within rounding. n = 48 scenes (12 years × 4 dry-season scenes; Landsat 8/9, WRS-2 path 164 / row 070; one least-cloudy acquisition per target month). Fitted slopes and the ratio of the endpoint means are not identical, because the annual series are not linear; both quantities are reported. For the vegetation class the 95% confidence interval includes zero, in agreement with the non-significant Mann–Kendall result.

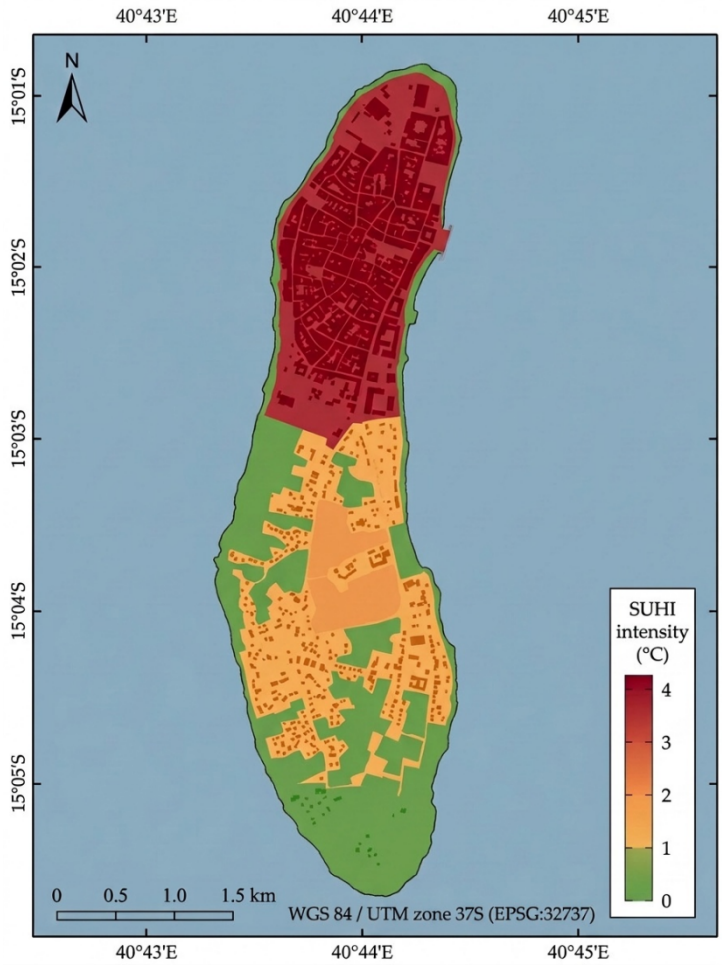


Figure 7. Maps mean SUHI intensity for the study period, defined as urban LST minus the land-vegetated reference. The heritage core is a persistent heat source, with intensities of 3–4 °C, while Macuti Town shows intermediate values of 1.5–2.5 °C. Coordinates are plotted on all four sides of the frame, the north arrow is in the upper left and the scale bar is below the frame.

3.3. Land Cover Relationships

Table 9 gives the correlations between land-cover characteristics and LST, computed on zonal means (12 years × 6 land-cover zones; effective sample size Neff = 72). Built-up fraction has the strongest positive correlation with LST (r = +0.72) and dense built-up an even stronger one (r = +0.84); vegetation cover correlates negatively (r = −0.68), as does NDVI (r = −0.65). Areas with more than 40% vegetation cover remained 2.5–3.8 °C below the island-wide mean LST. Because the coefficients rest on zonal means, the *p*-values in Table 9 are bounded by the number of zones and are reported as indicative; spatial dependence was tested separately with Moran's I (Table 6) and is discussed in Section 4.4.

Table 9. Correlation analysis between land-cover characteristics and land-surface temperature on Mozambique Island (zonal means).

Land Cover Variable	Correlation (r)	*p*-Value	Temperature Effect
Built-up area percentage	+0.72	<0.001	Positive correlation with elevated LST
Dense built-up areas	+0.84	<0.001	Strong positive correlation with high LST
Vegetation coverage	−0.68	<0.001	2.5–3.8 °C cooling effect
NDVI (vegetation index)	−0.65	<0.001	Higher NDVI = reduced LST
Stone/masonry construction	+0.58	<0.01	2.1 °C warmer than traditional materials
Distance from shoreline	+0.42	<0.05	Warmer away from the shore: +0.3 °C per 100 m (within 200 m of the coast)

Note: correlations computed on zonal means; *p*-values are indicative given the limited number of independent thermal footprints.

Stone and masonry areas averaged 2.1 °C warmer than areas of macuti and timber construction, an association observed in the satellite data rather than a controlled comparison. Distance from the shoreline correlates positively with LST (r = +0.42): pixels further from the coast were slightly warmer, at an indicative rate of about +0.3 °C per

100 m, and only within roughly 200 m of the coast, beyond which land cover dominates. Distance is measured from the high-water line, so a positive coefficient denotes warming as distance inland increases. Within a 100 m thermal footprint the coastal signal is averaged over two or three resident footprints and is therefore weak, so this gradient should be read with caution.

4. Discussion

4.1. SUHI in a Small Coastal Heritage Town

The main result is that a small island town sustains a measurable SUHI. The maximum intensity of 4.1 °C between the heritage core and the vegetated reference is of the same order as values reported for larger coastal cities in the region, such as Stone Town in Zanzibar (about 3.8 °C) and coastal settlements in Tanzania (2.9–4.5 °C) [87–89]. That a district a few hundred metres wide produces an effect of this magnitude shows how strongly urban fabric can modify the local surface climate, a control that is known to vary with the background climate of a city [90] and across biomes [91].

The 2.1 °C difference between the two districts is the most policy-relevant finding. It is consistent with their materials and vegetation: stone and lime mortar store heat during the day and release it slowly, whereas palm thatch and timber conduct heat less readily [92–94]. The result is an association, not a proof. The data cannot separate the effect of materials from that of density or vegetation, and no material-level or albedo measurements were made, so the inference remains descriptive until a multivariable model and direct observations of thermal mass, albedo and anthropogenic heat are available.

Vegetation cooling of 2.5–3.8 °C is in line with other tropical studies and points to green infrastructure as the most practical lever for thermal management in the heritage core, where vegetation covers less than 15% of the area [95–100]. For conservation this is important because repeated thermal cycling and high temperatures accelerate the weathering of limestone and coral stone [23,101–103]. The scale of the observation should be kept in mind: a neighbourhood-scale signal does not describe monument-scale thermal behaviour.

4.2. Temporal Trends and Their Interpretation

The island warmed at +0.148 °C yr^{-1} and the heritage core at +0.180 °C yr^{-1} (Table 8). Both rates lie above the two regional references used here: the published air-temperature trend for coastal northern Mozambique of about +0.08 °C yr^{-1} over a comparable period [88], and a 5 km × 5 km open-ocean LST reference computed from the same scenes, which warms at +0.05 °C yr^{-1} and contains no built surface. Multi-sensor comparisons of this kind are established practice in urban thermal studies [104], and remote sensing has long been used to relate land-cover change to surface temperature at scales comparable to this one [105]. The island trend is therefore consistent with a local surface-warming contribution on top of the regional signal, but the difference cannot be attributed to urban development alone, given the dry-season sampling schedule and the 100 m thermal support, and urbanisation has been shown to modify regional climate elsewhere [106].

Interpretation limits: the series covers the dry season only; it rests on four scenes per year; and the two sensors are not identical, although Band 11 was excluded uniformly and the atmospheric correction uses the same NASA ACCP source for every scene, so cross-sensor bias should be small [55]. A dry-season satellite series cannot by itself show that urban development caused the warming, nor separate that effect from changing acquisition conditions or the regional climate [107,108], which is the difficulty that urban-rural trend comparisons in other cities have also faced [109].

4.3. Implications for Heritage Conservation and Planning

The elevated temperatures in Stone and Lime Town are a conservation concern. Heat accelerates the chemical weathering of limestone and coral stone, and daily thermal cycling stresses masonry and mortar joints [23,101–103,110,111]. The mechanisms invoked here are documented for limestone and coral-stone building materials in general rather than measured on this island, where no material sampling or surface-energy-balance measurements were made. The historical fabric also offers a passive-cooling opportunity: courtyards, verandas and window placement were climate adaptations long before air conditioning and can be maintained without compromising authenticity [108,112–114].

In Macuti Town, the lower SUHI intensity associated with traditional materials and more vegetation suggests that vernacular construction is well adapted to the local climate [94,115,116]. The main risk is modernisation that replaces these materials with worse-performing ones, so planning policy should weigh thermal performance alongside other criteria [110,111]. Urban form itself, rather than individual materials, is a recognised control on the intensity of the heat island [117].

The island's small size cuts both ways. There is little room for large green infrastructure, but the compact form means that a few well-placed measures—strategic tree planting, higher-albedo surfaces, and passive-cooling design—could affect the whole town [96,118–121].

4.4. Limitations

Four limitations frame what can be concluded. (i) The native thermal support of Landsat Band 10 is 100 m and the distributed grid is a 30 m resampling. The island is 200–500 m wide, so only two to five independent thermal footprints cross it at any point; resampling does not create new spatial information [30,47,56], and thermal downscaling cannot recover detail that was never measured [122–124]. Coastal and narrow built-up pixels mix land, buildings and sea within a single footprint, and the data cannot reliably distinguish individual building materials, monument-scale thermal behaviour, fine urban morphology, small vegetation patches or a precise cooling threshold within the first 200 m of the coast. (ii) The data are daytime and dry-season only, so nighttime conditions and the full annual cycle are not covered. (iii) No ground-based validation was possible, so absolute temperatures carry the uncertainty of the atmospheric correction (NASA ACCP uncertainty in τ, L↑ and L↓ documented in Barsi et al. [69,70]). (iv) Attribution of the trend to urban development rather than to regional climate change is descriptive only, because the dry-season schedule prevents a strict causal reading.

The acquisition dates in Table 1 also drift slightly across the record, from a mean day-of-year of 197 in 2013 to 202 in 2024 (about half a day per year, five days in total), so a small seasonal sampling drift cannot be excluded as a minor contributor to the fitted trend. Other urban climate effects, such as the influence of urban surfaces on precipitation, are outside the scope of this dataset [125]. A permanent temperature monitoring network on the island would address most of these limitations and would support future higher-resolution thermal surveys, with ASTER or airborne thermal imagery [126,127]. Until such data exist, the conclusions describe patterns at the zonal scale of districts and neighbourhoods.

5. Conclusions

This study provides the first satellite-based thermal assessment of Mozambique Island, based on a twelve-year Landsat 8/9 archive processed in a single chain. Mean LST was 31.2 °C in Stone and Lime Town and 29.1 °C in Macuti Town, a persistent 2.1 °C contrast across the study period. The maximum SUHI intensity between the heritage core and the land-vegetated reference reached 4.1 °C in 2024, against about 2.8 °C in the early years of the record. Island-wide LST rose by +0.148 °C yr^{-1} (95% CI +0.080 to +0.216) and the heritage core at +0.180 °C yr^{-1} (95% CI +0.099 to +0.261). Built-up fraction was the strongest positive correlate of LST ($r = +0.72$) and vegetation cover the strongest negative correlate ($r = -0.68$).

Heritage managers and urban planners now have a quantitative baseline for the island. The wider point is that even a very small heritage settlement can sustain a measurable surface heat island, which remote sensing can detect where ground-based monitoring is impractical [114]. Urban heat also has direct consequences for human health during heat episodes [128]. Three caveats constrain that generalisation (Section 4.4), although the baseline itself is robust to the archive and to the definition of the reference zone (Section 2.5).

Software and Packages

All analyses were performed in R version 4.3.2 (R Foundation for Statistical Computing, 2023). Table 10 lists the software and package versions used, and the file manifest with checksums accompanies the reproducibility supplement.

Table 10. Software and package versions used in this study.

Tool	Version	Purpose	Reference
R	4.3.2	Statistical language	R Core Team (2023)
raster	3.6-26	Raster I/O and manipulation	https://cran.r-project.org/package=raster (accessed on May 2026)
sf	1.0-12	Vector data handling	https://cran.r-project.org/package=sf (accessed on May 2026)
caret	6.0-94	Classification and regression training	https://cran.r-project.org/package=caret (accessed on May 2026)
zyp	1.1-2	Sen's slope plus Mann–Kendall trend tests	https://cran.r-project.org/package=zyp (accessed on May 2026)
spdep	1.2-8	Spatial autocorrelation (Moran's I)	https://cran.r-project.org/package=spdep (accessed on May 2026)
QGIS	3.34 "Prizren"	Geographic information system	https://qgis.org (accessed on June 2026)
QGIS SCP plugin	7.10.4	Semi-Automatic Classification Plugin	https://plugins.qgis.org/plugins/SemiAutomaticClassificationPlugin/ (accessed on June 2026)
NASA ACCP	(web service; accessed 2026)	Atmospheric parameters (τ, L↑, L↓, T_air, RH, elevation)	Barsi and co-authors (2003, 2005); https://atmcorr.gsfc.nasa.gov/ (accessed on May 2026)

Supplementary Materials

The additional data and information can be downloaded at: https://media.sciltp.com/articles/others/261027141825655 3/UESD-26070153-SI.pdf. Table S1: Scene inventory of the 48 Landsat acquisitions (date, UTC overpass, cloud cover). Table S2: Atmospheric parameters applied to each scene. Table S3: Atmospheric parameters by acquisition month. Table S4: Classification accuracy of the five composites. Table S5: Confusion matrix of the 2024 composite. Table S6: Spatial autocorrelation (Moran's I) of the LST residuals. Table S7: Land-surface temperature statistics by district and land-cover class. Table S8: Trends in annual mean LST, 2013–2024. Table S9: Correlations between land-cover characteristics and LST (zonal means). Table S10: Software and package versions. Table S11: Annual mean LST by district and land-cover class, 2013–2024. Table S12: Zonal LST matrix, 12 years × 5 zones. Table S13: Scene-level acquisition and processing metadata. Table S14: Per-class accuracy of the 2024 composite.

Funding

This research received no external funding.

Institutional Review Board Statement

Not applicable.

Informed Consent Statement

Not applicable.

Data Availability Statement

The Landsat 8 and 9 imagery are publicly available from the USGS EarthExplorer (https://earthexplorer.usgs.gov/), Collection 2 Level-1, path 164, row 070, 2013–2024. The atmospheric parameters were obtained from the NASA Atmospheric Correction Parameter Calculator (https://atmcorr.gsfc.nasa.gov/) using the island centroid (15°02′ S, 40°44′ E) and the UTC acquisition time of each scene, and can be recomputed there. The reproducibility supplement is deposited in the Zenodo open-access repository under https://doi.org/10.5281/zenodo.22674203 and licensed CC-BY-4.0; it contains the 48-scene inventory and the R 4.3.2 scripts that reproduce the retrieval, trend and validation steps. The per-scene atmospheric parameters are listed in the Supplementary Information, which accompanies this paper under the same DOI and licence.

Acknowledgments

The author thanks the National Directorate of Territorial Planning (DINAT) of Mozambique for the administrative boundaries used in Figure 1, and acknowledges the OpenStreetMap contributors and Natural Earth for the data and basemap used under open licences. Landsat 8/9 Collection 2 Level-1 imagery from the USGS EarthExplorer archive and atmospheric parameters from the NASA Atmospheric Correction Parameter Calculator are gratefully acknowledged.

Conflicts of Interest

The author declares no conflict of interest.

Use of AI and AI-Assisted Technologies

AI-based tools were used for language editing and for formatting the references and tables. Scene selection, atmospheric correction, classification, the trend and correlation analyses and their interpretation were carried out and verified by the author, who takes full responsibility for the content of the manuscript.

References

1. Oke, T.R.; Mills, G.; Christen, A.; et al. *Urban Climates*; Cambridge University Press: Cambridge, UK, 2017; 525p. ISBN: 978-0-521-84950-0. https://doi.org/10.1017/9781139016476.
2. Santamouris, M. Recent progress on urban overheating and heat island research. Integrated assessment of the energy, environmental, vulnerability and health impact. Synergies with the global climate change. *Energy Build.* **2020**, *207*, 109482. https://doi.org/10.1016/j.enbuild.2019.109482.

3. Li, D.; Bou-Zeid, E. Synergistic Interactions between Urban Heat Islands and Heat Waves: The Impact in Cities Is Larger than the Sum of Its Parts. *J. Appl. Meteorol. Climatol.* **2013**, *52*, 2051–2064. https://doi.org/10.1175/jamc-d-13-02.1.
4. Stewart, I.D.; Oke, T.R. Local Climate Zones for Urban Temperature Studies. *Bull. Am. Meteorol. Soc.* **2012**, *93*, 1879–1900. https://doi.org/10.1175/bams-d-11-00019.1.
5. Mirzaei, P.A.; Haghighat, F. Approaches to study Urban Heat Island—Abilities and limitations. *Build. Environ.* **2010**, *45*, 2192–2201. https://doi.org/10.1016/j.buildenv.2010.04.001.
6. Gartland, L. *Heat Islands: Understanding and Mitigating Heat in Urban Areas*; Earthscan: London, UK, 2011; 192p. ISBN: 978-1-84971-298-9.
7. Weng, Q.; Lu, D.; Schubring, J. Estimation of land surface temperature–vegetation abundance relationship for urban heat island studies. *Remote Sens. Environ.* **2004**, *89*, 467–483. https://doi.org/10.1016/j.rse.2003.11.005.
8. Voogt, J.A.; Oke, T.R. Thermal remote sensing of urban climates. *Remote Sens. Environ.* **2003**, *86*, 370–384. https://doi.org/10.1016/s0034-4257(03)00079-8.
9. Song, J.; Du, S.; Feng, X.; et al. The relationships between landscape compositions and land surface temperature: Quantifying their resolution sensitivity with spatial regression models. *Landsc. Urban Plan.* **2014**, *123*, 145–157. https://doi.org/10.1016/j.landurbplan.2013.11.014.
10. Zhou, D.; Xiao, J.; Bonafoni, S.; et al. Satellite Remote Sensing of Surface Urban Heat Islands: Progress, Challenges, and Perspectives. *Remote Sens.* **2019**, *11*, 48. https://doi.org/10.3390/rs11010048.
11. Ramamurthy, P.; Pena, J.C.; Liu, S.; et al. The interaction between urban heat island intensity and sea-breeze effect. *Philos. Trans. R. Soc. A Math. Phys. Eng. Sci.* **2025**, *383*, 20240578. https://doi.org/10.1098/rsta.2024.0578.
12. Theeuwes, N.E.; Solcerová, A.; Steeneveld, G.J. Modeling the influence of open water surfaces on the summertime temperature and thermal comfort in the city. *J. Geophys. Res. Atmos.* **2013**, *118*, 8881–8896. https://doi.org/10.1002/jgrd.50704.
13. Martilli, A.; Clappier, A.; Rotach, M.W. An Urban Surface Exchange Parameterisation for Mesoscale Models. *Bound. Layer Meteorol.* **2002**, *104*, 261–304. https://doi.org/10.1023/a:1016099921195.
14. Nasar-u-Minallah, M.; Abdullah, M.; Fatima, N. Determinants of Urban Warming and Ecological Footprints in Lahore: Public Perceptions and Strategies for a Sustainable Future. *Forman J. Soc. Sci.* **2025**, *5*, 1–46. https://doi.org/10.32368/fjss.20250540.
15. Nasar-u-Minallah, M.; Jabeen, M.; Parveen, N.; et al. Exploring the seasonal variability and nexus between urban air pollution and urban heat islands in Lahore, Pakistan. *Acta Geophys.* **2025**, *73*, 3699–3719. https://doi.org/10.1007/s11600-025-01574-w.
16. Sattar, T.; Mirza, N.F.; Javed, M.A.; et al. Changing pattern of urban landscape and its impact on thermal environment of Lahore; Implications for climate change and sustainable development. *Environ. Monit. Assess.* **2025**, *197*, 151. https://doi.org/10.1007/s10661-024-13559-1.
17. Nasar-u-Minallah, M.; Haase, D.; Qureshi, S.; et al. Ecological monitoring of urban thermal field variance index and determining the surface urban heat island effects in Lahore, Pakistan. *Environ. Monit. Assess.* **2023**, *195*, 1212. https://doi.org/10.1007/s10661-023-11799-1.
18. Nasar-u-Minallah, M.; Haase, D.; Qureshi, S. Evaluating the impact of landscape configuration, patterns and composition on land surface temperature: An urban heat island study in the Megacity Lahore, Pakistan. *Environ. Monit. Assess.* **2024**, *196*, 627. https://doi.org/10.1007/s10661-024-12758-0.
19. Nasar-u-Minallah, M.; Jabbar, M.; Zia, S.; et al. Assessing and anticipating environmental challenges in Lahore, Pakistan: Future implications of air pollution on sustainable development and environmental governance. *Environ. Monit. Assess.* **2024**, *196*, 865. https://doi.org/10.1007/s10661-024-12925-3.
20. Jabbar, M.; Nasar-u-Minallah, M.; Yusoff, M.M. Predicting the Impact of Land Use Changes on Thermal Environment in Lahore, Pakistan: Implications for Urban Planning. *Geogr. Environ. Sustain.* **2024**, *17*, 95–109. https://doi.org/10.24057/2071-9388-2023-2862.
21. Derdouri, A.; Wang, R.; Murayama, Y.; et al. Understanding the Links between LULC Changes and SUHI in Cities: Insights from Two-Decadal Studies (2001–2020). *Remote Sens.* **2021**, *13*, 3654. https://doi.org/10.3390/rs13183654.
22. Emmanuel, R.; Krüger, E. Urban heat island and its impact on climate change resilience in a shrinking city: The case of Glasgow, UK. *Build. Environ.* **2012**, *53*, 137–149. https://doi.org/10.1016/j.buildenv.2012.01.020.
23. Bonazza, A.; Sardella, A.; Kaiser, A.; et al. Safeguarding cultural heritage from climate change related hydrometeorological hazards in Central Europe. *Int. J. Disaster Risk Reduct.* **2021**, *63*, 102455. https://doi.org/10.1016/j.ijdrr.2021.102455.
24. Sesana, E.; Gagnon, A.S.; Bertolin, C.; et al. Adapting Cultural Heritage to Climate Change Risks: Perspectives of Cultural Heritage Experts in Europe. *Geosciences* **2018**, *8*, 305. https://doi.org/10.3390/geosciences8080305.
25. Fabbri, K.; Pretelli, M. Heritage buildings and historic microclimate without HVAC technology: Malatestiana Library in Cesena, Italy, UNESCO Memory of the World. *Energy Build.* **2014**, *76*, 15–31. https://doi.org/10.1016/j.enbuild.2014.02.051.
26. Moonen, P.; Defraeye, T.; Dorer, V.; et al. Urban Physics: Effect of the micro-climate on comfort, health and energy demand. *Front. Archit. Res.* **2012**, *1*, 197–228. https://doi.org/10.1016/j.foar.2012.05.002.
27. Ketterer, C.; Matzarakis, A. Human-biometeorological assessment of heat stress reduction by replanning measures in Stuttgart, Germany. *Landsc. Urban Plan.* **2014**, *122*, 78–88. https://doi.org/10.1016/j.landurbplan.2013.11.003.

28. Sobrino, J.A.; Jiménez-Muñoz, J.C.; Paolini, L. Land surface temperature retrieval from LANDSAT TM 5. *Remote Sens. Environ.* **2004**, *90*, 434–440. https://doi.org/10.1016/j.rse.2004.02.003.
29. Jiménez-Muñoz, J.C.; Sobrino, J.A.; Skokovic, D.; et al. Land Surface Temperature Retrieval Methods from Landsat-8 Thermal Infrared Sensor Data. *IEEE Geosci. Remote Sens. Lett.* **2014**, *11*, 1840–1843. https://doi.org/10.1109/lgrs.2014.2312032.
30. Gillespie, A.; Rokugawa, S.; Matsunaga, T.; et al. A temperature and emissivity separation algorithm for Advanced Spaceborne Thermal Emission and Reflection Radiometer (ASTER) images. *IEEE Trans. Geosci. Remote Sens.* **1998**, *36*, 1113–1126. https://doi.org/10.1109/36.700995.
31. Li, X.; Stringer, L.C.; Chapman, S.; et al. How urbanisation alters the intensity of the urban heat island in a tropical African city. *PLoS ONE* **2021**, *16*, e0254371. https://doi.org/10.1371/journal.pone.0254371.
32. Garuma, G.F. Tropical surface urban heat islands in east Africa. *Sci. Rep.* **2023**, *13*, 4509. https://doi.org/10.1038/s41598-023-31678-6.
33. Bokaie, M.; Zarkesh, M.K.; Arasteh, P.D.; et al. Assessment of Urban Heat Island based on the relationship between land surface temperature and Land Use/ Land Cover in Tehran. *Sustain. Cities Soc.* **2016**, *23*, 94–104. https://doi.org/10.1016/j.scs.2016.03.009.
34. Agathangelidis, I.; Cartalis, C.; Santamouris, M. Urban Morphological Controls on Surface Thermal Dynamics: A Comparative Assessment of Major European Cities with a Focus on Athens, Greece. *Climate* **2020**, *8*, 131. https://doi.org/10.3390/cli8110131.
35. Tran, D.X.; Pla, F.; Latorre-Carmona, P.; et al. Characterizing the relationship between land use land cover change and land surface temperature. *ISPRS J. Photogramm. Remote Sens.* **2017**, *124*, 119–132. https://doi.org/10.1016/j.isprsjprs.2017.01.001.
36. Peng, S.; Piao, S.; Ciais, P.; et al. Surface Urban Heat Island Across 419 Global Big Cities. *Environ. Sci. Technol.* **2012**, *46*, 696–703. https://doi.org/10.1021/es2030438.
37. Azhar, R.; Javed, M.A.; Nasar-u-Minallah, M.; et al. Urban transformation in Lahore: Three decades of land cover changes, green space decline, and sustainable development challenges. *Geogr. Environ. Sustain.* **2024**, *17*, 6–17. https://doi.org/10.24057/2071-9388-2024-3204.
38. Duarte, R.T.; Meneses, M.P. The Archaeology of Mozambique Island. In *Aspects of African Archaeology: Papers from the 10th Congress of the Pan-African Association for Prehistory and Related Studies*; Pwiti, G., Soper, R., Eds.; University of Zimbabwe Publications: Harare, Zimbabwe, 1996; pp. 555–559.
39. Macamo, S.; Raimundo, M.Â.; Moffett, A.; et al. Developing Heritage Preservation on Ilha de Moçambique Using a Historic Urban Landscape Approach. *Heritage* **2024**, *7*, 2011–2030. https://doi.org/10.3390/heritage7040095.
40. Raimundo, M.Â.; Alcolete, I.; Macamo, S. The Integrity and Authenticity Challenge in the Protection of Mozambique Island, a UNESCO World Heritage Site: A Community-Centred Approach Aligned with the Nairobi Outcome. In *Heritage Authenticity in Theory and Practice in Africa*; Springer Nature Singapore: Singapore, 2026; pp. 119–133. https://doi.org/10.1007/978-981-92-2619-1_9.
41. UNESCO World Heritage Centre. *Operational Guidelines for the Implementation of the World Heritage Convention*; UNESCO World Heritage Centre: Paris, France, 2023.
42. Chaudhry, P.; Bagra, K.; Singh, B. Urban Greenery Status of Some Indian Cities: A Short Communication. *Int. J. Environ. Sci. Dev.* **2011**, *2*, 98–101. https://doi.org/10.7763/ijesd.2011.v2.104.
43. Valente Monteiro, C.; Lage, L.; Dal Cin, F.; et al. Preserving Coastal Heritage: A Review of Climate Adaptation Strategies on Ilha de Moçambique (Mozambique). *Land* **2025**, *14*, 1917. https://doi.org/10.3390/land14091917.
44. Manyilizu, M.; Dufois, F.; Penven, P.; et al. Interannual variability of sea surface temperature and circulation in the tropical western Indian Ocean. *Afr. J. Mar. Sci.* **2014**, *36*, 233–252. https://doi.org/10.2989/1814232x.2014.928651.
45. Lobato, A. *Ilha de Moçambique: Panorama Estético*; Junta de Investigações do Ultramar: Lisbon, Portugal, 1966; 126p.
46. Steyn, G. The Macuti Town on Mozambique Island in Context. *S. Afr. J. Art Hist.* **2025**, *40*, 66–79. https://doi.org/10.58978/sajah.2025.40.1.6.
47. Wu, H.; Li, Z.L. Scale Issues in Remote Sensing: A Review on Analysis, Processing and Modeling. *Sensors* **2009**, *9*, 1768–1793. https://doi.org/10.3390/s90301768.
48. Rapoport, A. *House Form and Culture; Foundations of Cultural Geography Series*; Prentice-Hall: Englewood Cliffs, NJ, USA, 1969; 146p. ISBN: 978-0-13-395673-3.
49. Kottek, M.; Grieser, J.; Beck, C.; et al. World Map of the Köppen-Geiger climate classification updated. *Meteorol. Z.* **2006**, *15*, 259–263. https://doi.org/10.1127/0941-2948/2006/0130.
50. Mahongo, S.B.; Shaghude, Y.W. Modelling the dynamics of the Tanzanian coastal waters. *J. Oceanogr. Mar. Sci.* **2014**, *5*, 1–7. https://doi.org/10.5897/joms2013.0100.
51. Reason, C.J.C.; Keibel, A. Tropical cyclone Eline and its unusual penetration and impacts over the southern African mainland. *Weather Forecast.* **2004**, *19*, 789–805. https://doi.org/10.1175/1520-0434(2004)019<0789:tceaiu>2.0.co;2.
52. USGS. *Landsat 8-9 Collection 2 Level-1 Data Product Guide*; U.S. Geological Survey: Reston, VA, USA, 2021.
53. Comia, H.R. Drought analysis in Pemba district, northern Mozambique (1991–2023) using the Standardized Precipitation Index (SPI). *Environ. Res. Commun.* **2026**, *8*, 035007. https://doi.org/10.1088/2515-7620/ae4aff.

54. Barsi, J.A.; Schott, J.R.; Hook, S.J.; et al. Landsat-8 Thermal Infrared Sensor (TIRS) Vicarious Radiometric Calibration. *Remote Sens.* **2014**, *6*, 11607–11626. https://doi.org/10.3390/rs61111607.
55. Schott, J.R.; Gerace, A.; Raqueno, N.; et al. Chasing the TIRS ghosts: Calibrating the Landsat 8 thermal bands. In Proceedings of the Earth Observing Systems XIX (SPIE Optical Engineering + Applications), San Diego, CA, USA, 17 August 2014; Vol. 9218, p. 92181A. https://doi.org/10.1117/12.2063236.
56. Wang, K.; Wan, Z.; Wang, P.; et al. Estimation of surface long wave radiation and broadband emissivity using Moderate Resolution Imaging Spectroradiometer (MODIS) land surface temperature/emissivity products. *J. Geophys. Res. Atmos.* **2005**, *110*, D11109. https://doi.org/10.1029/2004jd005566.
57. Becker, F.; Li, Z.L. Towards a local split window method over land surfaces. *Int. J. Remote Sens.* **1990**, *11*, 369–393. https://doi.org/10.1080/01431169008955028.
58. Tucker, C.J. Red and photographic infrared linear combinations for monitoring vegetation. *Remote Sens. Environ.* **1979**, *8*, 127–150. https://doi.org/10.1016/0034-4257(79)90013-0.
59. Sobrino, J.A.; Raissouni, N. Toward remote sensing methods for land cover dynamic monitoring: Application to Morocco. *Int. J. Remote Sens.* **2000**, *21*, 353–366. https://doi.org/10.1080/014311600210876.
60. Richards, J.A.; Jia, X. *Remote Sensing Digital Image Analysis: An Introduction*, 5th ed.; Springer Berlin Heidelberg: Berlin, Heidelberg, Germany, 2013; 494p. ISBN: 978-3-642-30061-5. https://doi.org/10.1007/978-3-642-30062-2.
61. Jiménez-Muñoz, J.C.; Cristóbal, J.; Sobrino, J.A.; et al. Revision of the Single-Channel Algorithm for Land Surface Temperature Retrieval from Landsat Thermal-Infrared Data. *IEEE Trans. Geosci. Remote Sens.* **2009**, *47*, 339–349. https://doi.org/10.1109/tgrs.2008.2007125.
62. Jiménez-Muñoz, J.C.; Sobrino, J.A. A generalized single-channel method for retrieving land surface temperature from remote sensing data. *J. Geophys. Res. Atmos.* **2003**, *108*, 4688. https://doi.org/10.1029/2003jd003480.
63. Chander, G.; Markham, B.L.; Helder, D.L. Summary of current radiometric calibration coefficients for Landsat MSS, TM, ETM+, and EO-1 ALI sensors. *Remote Sens. Environ.* **2009**, *113*, 893–903. https://doi.org/10.1016/j.rse.2009.01.007.
64. Markham, B.L. Landsat MSS and TM post-calibration dynamic ranges, exoatmospheric reflectances and at-satellite temperatures. *Landsat Tech. Notes* **1986**, *1*, 3–8.
65. Wukelic, G.E.; Gibbons, D.E.; Martucci, L.M.; et al. Radiometric calibration of Landsat Thematic Mapper thermal band. *Remote Sens. Environ.* **1989**, *28*, 339–347. https://doi.org/10.1016/0034-4257(89)90125-9.
66. Roy, D.P.; Wulder, M.A.; Loveland, T.R.; et al. Landsat-8: Science and product vision for terrestrial global change research. *Remote Sens. Environ.* **2014**, *145*, 154–172. https://doi.org/10.1016/j.rse.2014.02.001.
67. Montanaro, M.; Gerace, A.; Lunsford, A.; et al. Stray Light Artifacts in Imagery from the Landsat 8 Thermal Infrared Sensor. *Remote Sens.* **2014**, *6*, 10435–10456. https://doi.org/10.3390/rs61110435.
68. Planck, M. *The Theory of Heat Radiation*; P. Blakiston's Son & Co: Philadelphia, PA, USA, 1914; 244p.
69. Barsi, J.A.; Barker, J.L.; Schott, J.R. An atmospheric correction parameter calculator for a single thermal band earth-sensing instrument. In Proceedings of the IGARSS 2003: 2003 IEEE International Geoscience and Remote Sensing Symposium, Toulouse, France, 21–25 July 2003; Volume 5, pp. 3014–3016. https://doi.org/10.1109/igarss.2003.1294665.
70. Barsi, J.A.; Schott, J.R.; Palluconi, F.D.; et al. Validation of a web-based atmospheric correction tool for single thermal band instruments. In Proceedings of the SPIE 5882, Earth Observing Systems X, 58820E, San Diego, CA, USA, 31 July–1 August 2005; Vol. 5882, pp. 136–142. https://doi.org/10.1117/12.619990.
71. Mallick, J.; Singh, C.K.; Shashtri, S.; et al. Land surface emissivity retrieval based on moisture index from LANDSAT TM satellite data over heterogeneous surfaces of Delhi city. *Int. J. Appl. Earth Obs. Geoinf.* **2012**, *19*, 348–358. https://doi.org/10.1016/j.jag.2012.06.002.
72. Coll, C.; Caselles, V.; Galve, J.M.; et al. Ground measurements for the validation of land surface temperatures derived from AATSR and MODIS data. *Remote Sens. Environ.* **2005**, *97*, 288–300. https://doi.org/10.1016/j.rse.2005.05.007.
73. Schott, J.R.; Hook, S.J.; Barsi, J.A.; et al. Thermal infrared radiometric calibration of the entire Landsat 4, 5, and 7 archive (1982–2010). *Remote Sens. Environ.* **2012**, *122*, 41–49. https://doi.org/10.1016/j.rse.2011.07.022.
74. Congalton, R.G. A review of assessing the accuracy of classifications of remotely sensed data. *Remote Sens. Environ.* **1991**, *37*, 35–46. https://doi.org/10.1016/0034-4257(91)90048-b.
75. Anderson, J.R.; Hardy, E.E.; Roach, J.T.; et al. *A Land Use and Land Cover Classification System for Use with Remote Sensor Data*; US Geological Survey: Washington, DC, USA, 1976. https://doi.org/10.3133/pp964.
76. Foody, G.M. Status of land cover classification accuracy assessment. *Remote Sens. Environ.* **2002**, *80*, 185–201. https://doi.org/10.1016/s0034-4257(01)00295-4.
77. Thomlinson, J.R.; Bolstad, P.V.; Cohen, W.B. Coordinating Methodologies for Scaling Landcover Classifications from Site-Specific to Global: Steps toward Validating Global Map Products. *Remote Sens. Environ.* **1999**, *70*, 16–28. https://doi.org/10.1016/s0034-4257(99)00055-3.
78. Rouse, J.W.; Haas, R.H.; Schell, J.A.; et al. Monitoring vegetation systems in the Great Plains with ERTS. NASA: Washington, DC, USA, 1974.

79. Li, Z.L.; Tang, B.H.; Wu, H.; et al. Satellite-derived land surface temperature: Current status and perspectives. *Remote Sens. Environ.* **2013**, *131*, 14–37. https://doi.org/10.1016/j.rse.2012.12.008.
80. Mann, H.B. Nonparametric Tests against Trend. *Econometrica* **1945**, *13*, 245–259. https://doi.org/10.2307/1907187.
81. Pearson, K. VII. Note on regression and inheritance in the case of two parents. *Proc. R. Soc. Lond.* **1895**, *58*, 240–242. https://doi.org/10.1098/rspl.1895.0041.
82. DiBiase, D. *The Nature of Geographic Information: An Open Geospatial Textbook*; Penn State University: University Park, PA, USA, 2014.
83. R Core Team. *R: A Language and Environment for Statistical Computing*; R Foundation for Statistical Computing: Vienna, Austria, 2023.
84. Oke, T.R. The energetic basis of the urban heat island. *Q. J. R. Meteorol. Soc.* **1982**, *108*, 1–24. https://doi.org/10.1002/qj.49710845502.
85. Schwarz, N.; Lautenbach, S.; Seppelt, R. Exploring indicators for quantifying surface urban heat islands of European cities with MODIS land surface temperatures. *Remote Sens. Environ.* **2011**, *115*, 3175–3186. https://doi.org/10.1016/j.rse.2011.07.003.
86. Sen, P.K. Estimates of the Regression Coefficient Based on Kendall's Tau. *J. Am. Stat. Assoc.* **1968**, *63*, 1379–1389. https://doi.org/10.1080/01621459.1968.10480934.
87. Grimm, N.B.; Faeth, S.H.; Golubiewski, N.E.; et al. Global Change and the Ecology of Cities. *Science* **2008**, *319*, 756–760. https://doi.org/10.1126/science.1150195.
88. Kombe, W.J. Land use dynamics in peri-urban areas and their implications on the urban growth and form: The case of Dar es Salaam, Tanzania. *Habitat Int.* **2005**, *29*, 113–135. https://doi.org/10.1016/s0197-3975(03)00076-6.
89. Simon, O.; Yamungu, N.; Lyimo, J. Influence of Urban Land Use Land Cover Changes on Land Surface Temperature in Dar es Salaam Metropolitan City, Tanzania: The Use of Geospatial Approach. *Tanz. J. Sci.* **2023**, *49*, 356–368. https://doi.org/10.4314/tjs.v49i2.7.
90. Zhao, L.; Lee, X.; Smith, R.B.; et al. Strong contributions of local background climate to urban heat islands. *Nature* **2014**, *511*, 216–219. https://doi.org/10.1038/nature13462.
91. Imhoff, M.L.; Zhang, P.; Wolfe, R.E.; et al. Remote sensing of the urban heat island effect across biomes in the continental USA. *Remote Sens. Environ.* **2010**, *114*, 504–513. https://doi.org/10.1016/j.rse.2009.10.008.
92. Yuan, F.; Bauer, M.E. Comparison of impervious surface area and normalized difference vegetation index as indicators of surface urban heat island effects in Landsat imagery. *Remote Sens. Environ.* **2007**, *106*, 375–386. https://doi.org/10.1016/j.rse.2006.09.003.
93. Xiao, R.B.; Ouyang, Z.Y.; Zheng, H.; et al. Spatial pattern of impervious surfaces and their impacts on land surface temperature in Beijing, China. *J. Environ. Sci.* **2007**, *19*, 250–256. https://doi.org/10.1016/s1001-0742(07)60041-2.
94. Zoulia, I.; Santamouris, M.; Dimoudi, A. Monitoring the effect of urban green areas on the heat island in Athens. *Environ. Monit. Assess.* **2009**, *156*, 275–292. https://doi.org/10.1007/s10661-008-0483-3.
95. Bowler, D.E.; Buyung-Ali, L.; Knight, T.M.; et al. Urban greening to cool towns and cities: A systematic review of the empirical evidence. *Landsc. Urban Plan.* **2010**, *97*, 147–155. https://doi.org/10.1016/j.landurbplan.2010.05.006.
96. Ca, V.T.; Asaeda, T.; Abu, E.M. Reductions in air conditioning energy caused by a nearby park. *Energy Build.* **1998**, *29*, 83–92. https://doi.org/10.1016/s0378-7788(98)00032-2.
97. Carlson, T.N.; Ripley, D.A. On the relation between NDVI, fractional vegetation cover, and leaf area index. *Remote Sens. Environ.* **1997**, *62*, 241–252. https://doi.org/10.1016/s0034-4257(97)00104-1.
98. Grimmond, C.S.B.; Oke, T.R. Heat storage in urban areas: Local-scale observations and evaluation of a simple model. *J. Appl. Meteorol.* **1999**, *38*, 922–940. https://doi.org/10.1175/1520-0450(1999)038<0922:hsiual>2.0.co;2.
99. Saito, I.; Ishihara, O.; Katayama, T. Study of the effect of green areas on the thermal environment in an urban area. *Energy Build.* **1990**, *15*, 493–498. https://doi.org/10.1016/0378-7788(90)90026-f.
100. Gago, E.J.; Roldan, J.; Pacheco-Torres, R.; et al. The city and urban heat islands: A review of strategies to mitigate adverse effects. *Renew. Sustain. Energy Rev.* **2013**, *25*, 749–758. https://doi.org/10.1016/j.rser.2013.05.057.
101. Sailor, D.J. A review of methods for estimating anthropogenic heat and moisture emissions in the urban environment. *Int. J. Climatol.* **2011**, *31*, 189–199. https://doi.org/10.1002/joc.2106.
102. Akbari, H.; Pomerantz, M.; Taha, H. Cool surfaces and shade trees to reduce energy use and improve air quality in urban areas. *Sol. Energy* **2001**, *70*, 295–310. https://doi.org/10.1016/s0038-092x(00)00089-x.
103. Manohar, S.; Bala, K.; Santhanam, M.; et al. Characteristics and deterioration mechanisms in coral stones used in a historical monument in a saline environment. *Constr. Build. Mater.* **2020**, *241*, 118102. https://doi.org/10.1016/j.conbuildmat.2020.118102.
104. Dousset, B.; Gourmelon, F. Satellite multi-sensor data analysis of urban surface temperatures and landcover. *ISPRS J. Photogramm. Remote Sens.* **2003**, *58*, 43–54. https://doi.org/10.1016/s0924-2716(03)00016-9.
105. Chen, X.L.; Zhao, H.M.; Li, P.X.; et al. Remote sensing image-based analysis of the relationship between urban heat island and land use/cover changes. *Remote Sens. Environ.* **2006**, *104*, 133–146. https://doi.org/10.1016/j.rse.2005.11.016.

106. Zhou, L.; Dickinson, R.E.; Tian, Y.; et al. Evidence for a significant urbanization effect on climate in China. *Proc. Natl. Acad. Sci. USA* **2004**, *101*, 9540–9544. https://doi.org/10.1073/pnas.0400357101.
107. Winkler, E.M. *Stone in Architecture: Properties, Durability*, 3rd ed.; Springer Berlin Heidelberg: Berlin, Heidelberg, Germany, 1997; 313p. ISBN: 978-3-540-57626-6. https://doi.org/10.1007/978-3-662-10070-7.
108. Santamouris, M.; Kolokotsa, D. Passive cooling dissipation techniques for buildings and other structures: The state of the art. *Energy Build.* **2013**, *57*, 74–94. https://doi.org/10.1016/j.enbuild.2012.11.002.
109. Stone, B. Urban and rural temperature trends in proximity to large US cities: 1951–2000. *Int. J. Climatol.* **2007**, *27*, 1801–1807. https://doi.org/10.1002/joc.1555.
110. Sabbioni, C.; Brimblecombe, P.; Cassar, M. *The Atlas of Climate Change Impact on European Cultural Heritage: Scientific Analysis and Management Strategies*; Anthem Press: London, UK, 2010; 160p. ISBN: 978-1-84331-798-2.
111. Intergovernmental Panel on Climate Change (IPCC). *Climate Change 2021—The Physical Science Basis*; Cambridge University Press: Cambridge, UK, 2021; 2391p. ISBN: 978-1-009-15789-6. https://doi.org/10.1017/9781009157896.
112. Kong, F.; Yin, H.; James, P.; et al. Effects of spatial pattern of greenspace on urban cooling in a large metropolitan area of eastern China. *Landsc. Urban Plan.* **2014**, *128*, 35–47. https://doi.org/10.1016/j.landurbplan.2014.04.018.
113. Chang, C.R.; Li, M.H.; Chang, S.D. A preliminary study on the local cool-island intensity of Taipei city parks. *Landsc. Urban Plan.* **2007**, *80*, 386–395. https://doi.org/10.1016/j.landurbplan.2006.09.005.
114. Foruzanmehr, A.; Vellinga, M. Vernacular architecture: Questions of comfort and practicability. *Build. Res. Inf.* **2011**, *39*, 274–285. https://doi.org/10.1080/09613218.2011.562368.
115. Zhai, Z.J.; Previtali, J.M. Ancient vernacular architecture: Characteristics categorization and energy performance evaluation. *Energy Build.* **2010**, *42*, 357–365. https://doi.org/10.1016/j.enbuild.2009.10.002.
116. Bourdier, J.P.; Trinh, T. *Vernacular Architecture of West Africa: A World in Dwelling*; Routledge: London, UK, 2011; 192p. ISBN: 978-0-415-58543-9.
117. Stone, B.; Rodgers, M.O. Urban Form and Thermal Efficiency*:* How the Design of Cities Influences the Urban Heat Island Effect*. J. Am. Plan. Assoc.* **2001**, *67*, 186–198. https://doi.org/10.1080/01944360108976228.
118. Aguilar, E.; Aziz Barry, A.; Brunet, M.; et al. Changes in temperature and precipitation extremes in western central Africa, Guinea Conakry, and Zimbabwe, 1955–2006. *J. Geophys. Res. Atmos.* **2009**, *114*, D02115. https://doi.org/10.1029/2008jd011010.
119. Rydin, Y.; Bleahu, A.; Davies, M.; et al. Shaping cities for health: Complexity and the planning of urban environments in the 21st century. *Lancet* **2012**, *379*, 2079–2108. https://doi.org/10.1016/s0140-6736(12)60435-8.
120. Gill, S.E.; Handley, J.F.; Ennos, A.R.; et al. Adapting Cities for Climate Change: The Role of the Green Infrastructure. *Built Environ.* **2007**, *33*, 115–133. https://doi.org/10.2148/benv.33.1.115.
121. Takebayashi, H.; Moriyama, M. Surface heat budget on green roof and high reflection roof for mitigation of urban heat island. *Build. Environ.* **2007**, *42*, 2971–2979. https://doi.org/10.1016/j.buildenv.2006.06.017.
122. Zakšek, K.; Oštir, K. Downscaling land surface temperature for urban heat island diurnal cycle analysis. *Remote Sens. Environ.* **2012**, *117*, 114–124. https://doi.org/10.1016/j.rse.2011.05.027.
123. Leconte, F.; Bouyer, J.; Claverie, R.; et al. Using Local Climate Zone scheme for UHI assessment: Evaluation of the method using mobile measurements. *Build. Environ.* **2015**, *83*, 39–49. https://doi.org/10.1016/j.buildenv.2014.05.005.
124. Bechtel, B.; Zakšek, K.; Hoshyaripour, G. Downscaling Land Surface Temperature in an Urban Area: A Case Study for Hamburg, Germany. *Remote Sens.* **2012**, *4*, 3184–3200. https://doi.org/10.3390/rs4103184.
125. Lowry, W.P. Urban effects on precipitation amount. *Prog. Phys. Geogr. Earth Environ.* **1998**, *22*, 477–520. https://doi.org/10.1177/030913339802200403.
126. Arnfield, A.J. Two decades of urban climate research: A review of turbulence, exchanges of energy and water, and the urban heat island. *Int. J. Climatol.* **2003**, *23*, 1–26. https://doi.org/10.1002/joc.859.
127. Smith, B.J.; Gómez-Heras, M.; Viles, H.A. Underlying issues on the selection, use and conservation of building limestone. *Geol. Soc. Lond. Spec. Publ.* **2010**, *331*, 1–11. https://doi.org/10.1144/sp331.1.
128. Patz, J.A.; Campbell-Lendrum, D.; Holloway, T.; et al. Impact of regional climate change on human health. *Nature* **2005**, *438*, 310–317. https://doi.org/10.1038/nature04188.